Position-Domain Geometry Screening to Maximize LAAS Availability in the Presence of Ionosphere Anomalies

Jiyun Lee, Ming Luo, Sam Pullen, Young Shin Park and Per Enge

Stanford University

Mats Brenner

Honeywell Aerospace

ABSTRACT

All fault modes in the Local Area Augmentation System should be mitigated within the specified integrity risk allocation to guarantee the safety of a landing aircraft. However, monitoring within the LAAS Ground Facility is insufficient to completely protect users from unacceptable errors due to ionosphere spatial gradient anomalies. A methodology has been developed to inflate the broadcast σ_{pr_gnd} and σ_{vig} so that subset satellite geometries (i.e., subsets of the set of approved GPS satellites for which the LGF broadcasts valid corrections) for which unacceptable errors are possible are made unavailable to users. The required sigma inflation factors are computed offline and are input into each LGF site during site installation. These offline simulations and the resulting inflation factors are updated periodically to insure that they remain sufficient to mitigate residual ionosphere anomaly risk. This paper describes the updated ionosphere threat space and the geometry screening algorithm required to be implemented to support the FAA/Honeywell LAAS Provably Safe Prototype (PSP) at Memphis airport. It also demonstrates by simulation results that the required availability of integrity for CAT I approaches is achievable with the proposed method.

1.0 INTRODUCTION

The Local Area Augmentation System (LAAS) is designed to guarantee the integrity of each broadcast pseudorange correction by monitoring of measured satellite pseudoranges within the LAAS Ground Facility (LGF). This monitoring allows the LGF to ensure that the errors in LGF pseudorange corrections are bounded (to the required integrity probability) by the nominal error sigmas that are broadcast with them (within the LGF, measurements that fail one or more monitors are excluded so that they do not affect the broadcast parameters). This procedure allows aircraft receiving LAAS corrections to compute "protection levels" and thus determine the integrity of any set of satellites visible at the aircraft

While almost all anomalies that pose a threat to LAAS can be mitigated completely within the range domain, severe ionosphere spatial anomalies must be handled differently. Very large ionosphere spatial gradients observed in CONUS during ionosphere storms in October and November 2003 could have created range-domain errors of several meters before being detected by LGF monitoring [1, 2]. The magnitude of these potential errors exceeds what can be bounded in the range domain. In other words, aircraft satellite geometries that appear usable due to the vertical protection level (or VPL) being below the specified "safe" vertical alert limit (or VAL) for CAT I precision approaches (VAL = 10 meters at the minimum CAT I decision height of 200 ft) are usable with respect to nominal conditions and almost all failure modes but may not be safe in the presence of a worst-case ionosphere anomaly. Therefore, satellite geometry screening, or position-domain verification that each geometry potentially usable at the aircraft is safe in the presence of the ionosphere-anomaly threat, is required.

LGF position-domain verification produces an inflation factor that depends on the current satellite constellation. In fact, separate inflation factors are applied to the two broadcast sigma values (σ_{pr_gnd} and σ_{vig}) when the nominal sigma values do not produce a VPL that exceeds VAL when the possible error is not bounded by $VAL_{H2,I}$ (this "additional" VAL will be defined shortly). This inflation is done in off-line simulation known as "pre-screening". Prior to installation of a new LGF site, geometry-screening simulations are run to cover all possible GPS satellite constellations, times of day, airborne "subset" geometries (subsets of the set of satellites visible to and approved by a theoretical LGF), user-LGF separations, and ionosphere anomaly permutations given by the ionosphere threat model. Offline operation of this algorithm produces inflation factors for each case that is not sufficiently protected by range-domain monitoring. Since no means of knowing the current geometry condition would be available in real time, the highest level of inflation over all scenarios simulated in pre-screening would need to be applied by the LGF at all times. Real-time operation of a similar

algorithm can be chosen to provide the lowest inflation factors that cover the current geometries. A real-time approach would have higher availability than the offline method proposed in this paper (because the maximum inflation factors need not be used all the time) but would burden the LGF processor with a major additional computational task.

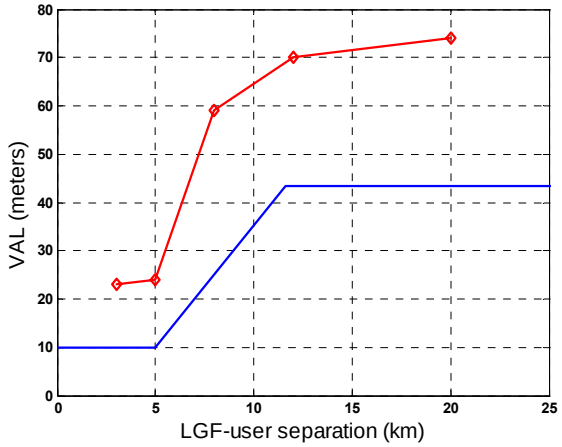

Figure 1: Example $VAL_{H2,I}$ Curve Originally Chosen for 99.9% Availability

It is important to understand the significance of $VAL_{H2,I}$ and how it differs from VAL. Because of the expected rarity of the worst-case ionosphere anomaly generated as part of geometry screening simulation, and because it is believed that vertical errors larger than the standard VAL can be experienced by Category I precision approach users with little or no additional risk (see [3]), it was decided that the ground system screening/monitoring function could use a higher maximum error bound than the broadcast Final Approach Segment (FAS)VAL of 10 meters for this particular anomaly condition. In other words, the maximum vertical position error (plus K_{MD} sigma of nominal error) due to the worst-case user error induced by an ionosphere anomaly (as estimated by the ground subsystem) need only be bounded by $VAL_{H2,I}$. During flight, users will compare their computed VPLs to the broadcast (standard) VAL as a function of FASVAL (FASVAL is broadcast, and VAL is derived from it as a function of aircraft location on the approach – see Table 2-13 of [4]), but the LGF will have determined the required broadcast sigma values based on the need to protect users from ionosphere anomalies that could cause worst-case errors exceeding $VAL_{H2,I}$. Figure 1 shows the example $VAL_{H2,I}$ curve that has been used in the current sigma inflation determination. The validation of such a curve is underway, and it may subject to future revisions. Therefore, the eventual $VAL_{H2,I}$ curve to be used for CAT I LAAS will be a set of input parameters to the offline simulation algorithm.

This paper demonstrates that position-domain geometry screening in LAAS can fully mitigate the CONUS ionosphere spatial decorrelation threat model. Section 2 presents the most recently updated threat model. Section 3 describes the method used to generate the worst-case aircraft differential range errors based on the established threat model, and it explains how range error look-up tables are created for use by the position-domain simulation.

Section 4 focuses on the design of the position-domain geometry screening simulation. It first explains how to propagate range-domain ionosphere-induced errors through all possible user subset geometries to obtain worst-case vertical errors. It also describes the sigma inflation algorithm that determines inflation factors for σ_{pr_gnd} and σ_{vig} required to protect against the worst-case ionosphere induced errors. Simulation results are presented in Section 5 with some discussion on the implementation of this algorithm. This work is summarized in Section 6.

2.0 IONOSPHERE THREAT MODEL

The ionosphere is a region of the atmosphere located about 50 – 1000 km above the Earth's surface. In this region, solar radiation produces free electrons and ions that cause phase advance and group delay to radio waves. If uncorrected, the error introduced by the ionosphere onto the GPS signal can be as high as tens of meters. Ionosphere delays on GPS pseudorange measurements normally are very highly correlated over short distances (to within 1 – 2 mm/km, one sigma). However, unusual solar-geomagnetic events such as Coronal Mass Ejections (CME) from the Sun can cause the ionosphere to behave anomalously. The extremely large gradients observed during the April 2000, October 2003, and November 2003 ionosphere storms were two orders of magnitude higher than the typical one-sigma ionosphere vertical gradient value mentioned above. Since a Gaussian extrapolation of the 4 mm/km one-sigma number planned to be broadcast by the LGF [5] does not come close to bounding these extreme gradients, we must treat these events as anomalies and detect or mitigate cases which might lead to hazardous user errors.

From the point of view of a user approaching a LAAS-equipped airport, an anomalous ionosphere gradient has been modeled as a linear semi-infinite wave front with constant propagation speed. The gradient is assumed to be a linear change in vertical ionosphere delay between maximum and minimum delays. The spatial gradient (slope) in slant (not zenith) ionosphere delay, the width of the linear change in delay, and the forward propagation speed of the wave front relative to the ground (assumed constant) are the three key parameters in the LAAS ionosphere threat model. Note that the maximum

ionosphere delay difference is the product of slope and width and is upper-bounded by a maximum value (see Table 1). Slope and width values that, when multiplied together, create a maximum delay difference above a certain bound are not part of the threat model. Figure 2 illustrates this simplified model of an ionosphere wave front.

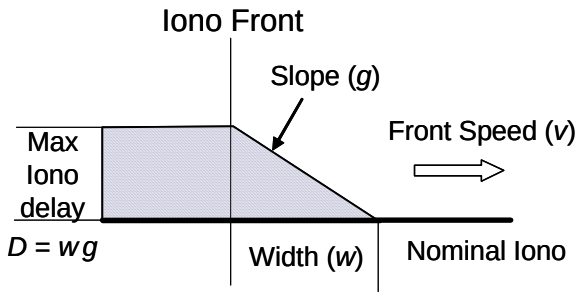

Figure 2: Ionosphere Wave Front Model

To establish upper and lower bounds on the three key parameters of the threat model, post-processed WAAS Supertruth data and data from the National Geodetic Survey Continuously Operating Reference Stations (NGS-CORS, or just CORS) network of receivers have been studied in detail [6]. A comprehensive methodology for ionosphere anomaly data assessment was developed over time to automatically search for anomalies and to estimate slopes and speeds of ionosphere fronts within the Conterminous United States (CONUS) region during days of severe ionosphere activity, also known as "ionosphere storm days" [7]. Because the measurements of ionosphere delay come from imperfect receivers whose ability to track GPS signals is also affected by severe ionosphere behavior (also, the post-processing technique is not perfect either), each apparent anomaly must be examined in order to determine whether it is caused by a real ionosphere event or, instead, results from faulty measurements. In order to overcome the problem of errors in the ionosphere data given to us, raw L1 code-minus-carrier (CMC) based on data downloaded directly from the CORS website [6] was used to generate approximate wave front parameter estimates, and these estimates were used to validate the L1/L2 observations [7]. Anomalous ionosphere events that pass this comparison are deemed to be "validated" measurements and are used to generate bounds on the threat model parameters.

Figure 3 shows the results of this data analysis process for satellites above 12 degrees elevation. Two zones of wave front speed are shown: "slow-moving" wave fronts below 90 m/s and "fast-moving" wave fronts above 90 m/s. Below 90 m/s, the maximum gradient discovered (in Florida on 31 October 2003) was about 100 mm/km in slant. Above 90 m/s, the maximum gradient discovered (in Ohio/Michigan on 20 November 2003) was just over 300 mm/km in slant. Error bars are shown to represent the uncertainty in both slope and speed estimates due to measurement errors and inconsistencies between the data and the constant linear threat model geometry. Note that width estimates do not appear in this figure because they are very difficult to assess given the typical 50 – 100 km separation of CORS reference stations. Fortunately, the impact of ionosphere wave fronts on LAAS is not very sensitive to width; thus the choice was made to include a range of possible front widths from 25 to 200 km in the threat model. Note that all front speeds in Figure 3 are expressed relative to the ground (e.g., relative to the fixed location of the LGF).

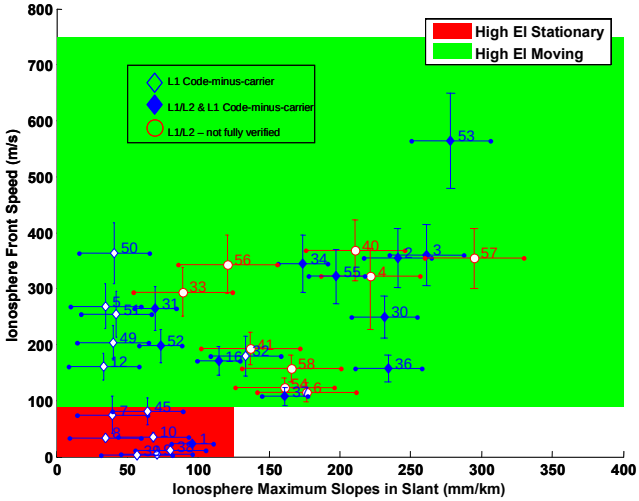

Figure 3: Anomalous Ionosphere Gradients Observed Above 12° Elevation

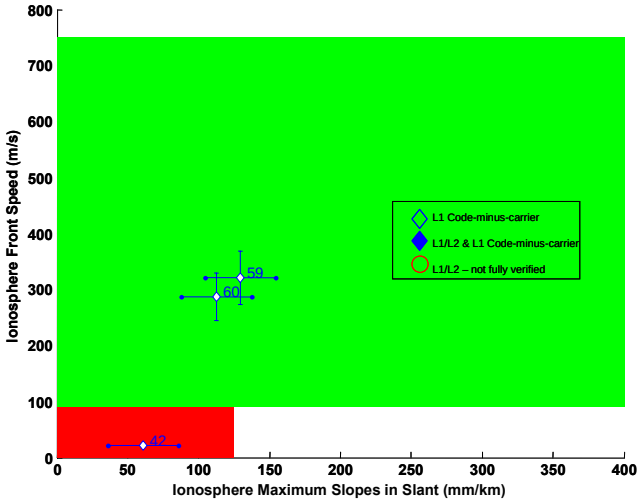

Figure 4: Anomalous Ionosphere Gradients Observed Below 12° Elevation

Figure 4 shows the limited number of validated events discovered for satellites below 12 degrees elevation. While CORS data contains measurements of satellites as

low as 5 degrees, not as many examples of satellites this low exist in CORS data, and the vast majority of these are noisy and/or contain multiple losses-of-lock and thus cannot be validated. The three validated events shown in Figure 4, along with the larger set of WAAS supertruth observations, suggest that the maximum gradient below 12° is 150 mm/km.

Elevation	Speed	Width	Slope (slant)	Max. Error
Low elevation (< 12°)	90 – 750 m/s	25 – 200 km	30 – 150 mm/km	30 m
	0 – 90 m/s	25 – 200 km	30 – 125 mm/km	25 m
High elevation (≥ 12°)	90 – 750 m/s	25 – 200 km	30 – 330 mm/km(†)	50 m(*)
	0 – 90 m/s	25 – 200 km	30 – 125 mm/km	25 m

(*) Max. error constrains possible slope/width combinations

(†) Max. gradient is a function of speed and elevation angle

Table 1: Ionosphere Spatial Gradient Threat Space Parameter Bounds

Table 1 represents one of the key results of this data-analysis process. Breaking the threat space into four regions based on front speed and satellite elevation, it shows the bounds on each of the three parameters in the ionosphere threat model for CAT I LAAS. In order to limit this threat model to the maximum gradients discovered and validated (plus margin for measurement error), empirical bounds were fitted to the results shown in Figures 3 and 4.

Previous study of the severe ionosphere storm of November 20, 2003 based on WAAS supertruth data showed a clear trend of decreasing gradient slope with decreasing elevation angle below 35° [8]. The scientific explanation of such phenomena has not been clear yet. However, it is decided to take this dependence into account in terms of the CAT I LAAS threat model. After combining the two boundaries (a slope bound as a function of front speed and a slope bound as a function of elevation angle) together, the exact values of the maximum ionosphere spatial gradients (denoted as *Slope*) allowed by the threat model are completely expressed by equation (1).

$$
\begin{aligned}
&Slope_{vel}(V_{front}) = 125; \quad V_{front} \le 90 \\
&Slope_{vel}(V_{front}) = \frac{(177-125)}{(108-90)}(V_{front}-90)+125; \quad 90 < V_{front} \le 108 \\
&Slope_{vel}(V_{front}) = \frac{(211-177)}{(115-108)}(V_{front}-108)+177; \quad 108 < V_{front} \le 115 \\
&Slope_{vel}(V_{front}) = \frac{(258-211)}{(158-115)}(V_{front}-115)+211; \quad 115 < V_{front} \le 158 \\
&Slope_{vel}(V_{front}) = \frac{(330-258)}{(354-158)}(V_{front}-158)+258; \quad 158 < V_{front} \le 354
\end{aligned}
\qquad (1)
$$

$$
\begin{aligned}
&Slope_{vel}(V_{front}) = 330; \quad V_{front} > 354 \\
&Slope_{el}(El) = \frac{(330-50)}{35}(El)+50; \quad El \le 35 \\
&Slope_{el}(El) = 330; \quad El \ge 35 \\
&Slope(V_{front}, El) = Min\,(Slope_{el}(El), Slope_{vel}(V_{front}))
\end{aligned}
$$

where El denotes the satellite elevation angle in degrees, and V_{front} denotes the ionosphere wave front propagation speed with respect to the ground. A specified gradient limit for each given front speed and a satellite elevation angle is established by taking the lower of the slope bound based on V_{front} (or $Slope_{vel}$) and the slope bound based on elevation angle (or $Slope_{el}$).

3.0 RANGE ERROR SIMULATION WITH CCD MONITOR

This section determines the worst-case airborne differential *range* errors in the presence of an anomalous ionosphere front within the threat model defined in Section 2.0. This worst-case aircraft differential range error is primarily determined by the limits enforced by monitoring in the LGF. The monitor that best mitigates the impact of the ionosphere front is the code-carrier divergence rate monitor (CCD). In this paper, only the CCD rate monitor as defined in [9] is assumed. In addition, the time from detection in the LGF to measurement exclusion in the aircraft is assumed to be 3 seconds. The resulting range errors are used in the LAAS ionosphere-anomaly impact simulation described in Section 4.0.

3.1 RANGE ERROR SIMULATION

The worst case differential range error for a particular gradient and relative velocity between the storm front and the ionosphere pierce point (IPP) is determined based on simulation. Note that the threat model in Section 2.0 expresses all front velocities relative to the ground so that they can be extrapolated back into satellite-observation space by adding the IPP velocity for a particular satellite. The simulation is set up so that both the LGF and the airborne system are outside the ionosphere front at the start of the simulation and the aircraft is over the "evaluation point" at the end of the simulation. The evaluation point is typically a point on the airport surface at or beyond the threshold corresponding to the decision height (DH) associated with an approach. The evaluation point is described by the threshold distance to the LGF and the distance from the evaluation point to the threshold. For a given gradient slope (G) and relative velocity (V) between front and IPP, the simulation searches through all possible combinations of front widths, (W) and relative positions (Δd) of front edge and airplane at the evaluation point to determine the worst-case differential range error. If detection by the CCD rate

Figure 5: Location of Airplane Relative to Front at Evaluation Point ($V > v_{air}$)

Figure 6: Location of Airplane relative to Front at Start Time ($V > v_{air}$)

monitor occurs prior to reaching the evaluation point, the satellite is assumed to be excluded by the LGF and is no longer used by the aircraft; thus the differential error is not reflected (included) in the worst-case differential error search.

Table 2 shows the parameter ranges and step sizes (or bin sizes) used in the airborne differential error simulation.

Threat Parameter	Min	Max	Step	Number of Steps
W (km)	25	200	2.5	70
V (m/s)	0	750	10	75
G (mm/km)	30	400	5	74
Δd (km)	–40	W +40	1	variable (100)

Table 2: Threat Parameter Ranges and Steps

The simulation is set up as follows. The last t_{run} seconds of the landing is simulated, and t_{run} is varied as needed to cover the essential part of the ionosphere front passage. The glideslope threshold is T km away from the LGF centroid. The evaluation point is located ΔD km away from the glideslope threshold T (and ΔD km further away from the LGF centroid). The evaluation point is thus located $D = T + \Delta D$ (km) relative to the LGF centroid. The airplane speed is assumed to be v_{air} = 70 m/s. The initial airplane position is:

$$d_{air}(0) = v_{air} \times t_{run} + D \quad . \qquad (2)$$

The airplane position as a function of time t is:

$$d_{air}(t) = d_{air}(0) - v_{air} \times t \quad . \qquad (3)$$

Meanwhile, the front is moving at speed V [m/s], has an ionosphere delay gradient of G [mm/km], and has a width of W [km]. The initial position of the front is $d_{front}(0)$. The position of the front as a function of time t is

$$d_{front}(t) = d_{front}(0) - V \times t \quad . \qquad (4)$$

Note that the maximum slant ionosphere delay from the threat model is 50 m (for fast-moving fronts affecting satellites above 12° elevation). Therefore, only threat model parameter combinations that meet $G \times W \leq 50$ m are included in this simulation. The threat model allows further restrictions of the parameter combinations, but to limit the scope of this simulation effort, these combinations were not excluded (these additional constraints are implemented when the results of this single-satellite range-domain simulation are used to build MIER and delta-V tables as inputs to follow-on position-domain simulations – see Section 3.2).

The simulation assumes a straight-in approach, and the front speed and the airplane speed are in the same direction. No other monitors than the CCD monitor are used in the LGF, and no monitors are assumed in the airborne. Initial conditions are set up differently depending on the following three cases:

a) $V > v_{air}$ (ionosphere front moves faster than airplane);

b) $V = v_{air}$ (ionosphere front moves at same speed as airplane);

c) $V < v_{air}$ (airplane moves faster than ionosphere front).

In case (a), where V is greater than v_{air}, the arrangement is as follows. We choose where the airplane will be relative to the front edge when it is located at the evaluation point (i.e., at the end of the simulation trial) as shown in Figure 5. The gray dot representing the airplane in Figure 5 is lifted up to indicate the ionosphere delay experienced at this point. The range of the relative distance Δd is [0, W + 40 km]. Next, move the ionosphere front and the airplane backwards. In other words, go backwards in time until the airplane is just in front of the ionosphere front zone, as shown in Figure 6. Based on the time needed for the

airplane to move from $d_{front}(0)$ at $t(0)$ to the evaluation point D at constant velocity v_{air}, one can calculate t_{run} and start the simulation to run from $t(0)$ to t_{run}. Range error simulations for cases (b) and (c) are done in a very similar manner as for case (a), and the details are described in [8].

For each user-threshold-LGF separation, the simulation provides the maximum differential range error (MIER – literally "maximum ionosphere error in range") for any ionosphere gradient and front speed relative to an IPP. Figure 7 shows simulation results for a user-to-LGF separation of 5 km. Note that the MIER results in Figure 7 are given by varying color levels, which are indexed by the color bar on the right-hand side of the plot. As the gradient G [mm/km] increases, MIER increases. As the front speed relative to the IPP increases, MIER decreases because the likelihood of CCD monitor detection increases.

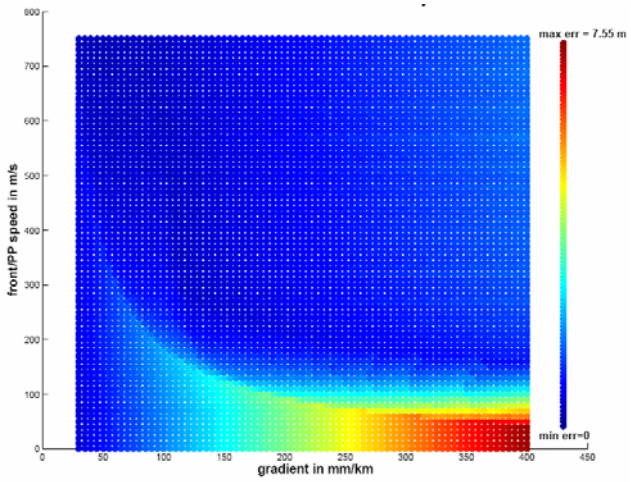

Figure 7: Example Results of Range-Error Simulation for Evaluation Point of 5 km from LGF

3.2 MIER AND DELTA-V LOOKUP TABLES

To reduce the number of permutations that must be checked in the geometry-screening algorithm described in Section 4.0, we create a series of tables, namely, maximum range error tables, $f_{Table}(dV_{front/IPP}, V_{front}, El)$, and delta-V tables, $dV_{Table}(V_{ipp}, El)$. These tables are used to identify the worst possible differential pseudorange error on a single satellite along with the conditions under which it occurs so that this worst-case scenario can be implemented within the position-domain simulation.

The Maximum Ionosphere-induced Error in Range (MIER) tables, $f_{Table}(dV_{front/IPP}, V_{front}, El)$, contain ionosphere-induced range errors as a function of the ionosphere front speed with respect to the ionosphere pierce point, $dV_{front/IPP}$, the ionosphere front speed with respect to the ground, V_{front}, and the satellite elevation angle, El. This table is generated using the ionosphere threat model established in Section 2.0 and the range-error simulation results described in Section 3.1. First, for a given V_{front} and El, the maximum ionosphere slope is determined from Equation (1). Second, a range-domain error is obtained from the range-error simulation results for a given gradient and $dV_{front/IPP}$. Thus, range errors can be computed for various values of $dV_{front/IPP}$ (within the range specified in the threat model) for a given V_{front} and elevation angle.

Delta-V tables, $dV_{Table}(V_{ipp}, El)$, contain $dV_{front/IPP}$ values that maximize the ionosphere-induced range errors as a function of the ionosphere pierce point speed, V_{ipp}, and satellite elevation angle, El. Delta-V tables are generated based upon the MIER tables described above (also see [8]). For each combination of V_{ipp} and elevation angle (both of which can be computed for each satellite visible to the LGF), a value of $dV_{front/IPP}$ can be found to correspond to the maximum range error in the three-dimensional range error table which covers the entire range of possible values of $dV_{front/IPP}$. Thus, the values of $dV_{front/IPP}$ are searched for any given combination of V_{ipp} and elevation angle to find the one that gives the maximum range error.

4.0 POSITION DOMAIN GEOMETRY SCREENING

Position-domain geometry screening consists of two parts: simulation to determine the Maximum-Ionosphere-induced-Error-in-Vertical (MIEV) as described in Sections 4.1 – 4.3 and determination of sigma inflation factors as described in Sections 4.4 – 4.7. The steps in Sections 4.1 – 4.3 are illustrated in the block diagrams of Figure 8 for the stationary-ionosphere-front scenario. Analogous steps are repeated for the fast-moving-ionosphere-front scenario. The steps in Section 4.4 and Sections 4.5 – 4.7 are illustrated in Figures 10 and 11, respectively.

4.1 AIRPORT AND SUBSET GEOMETRIES

The LGF generates all possible "subset" geometries from the all-in-view set of N approved satellites down to all four-satellite geometries that the aircraft theoretically might use. The maximum number of subsets, α, is

$$\alpha_N = \sum_{k=4}^{N} \binom{N}{k}. \quad (5)$$

If the two-satellites-impacted scenario is chosen for processing, all satellite pairs, $(k_1, k_2)_N$, must be identified for each subset geometry. The number of pairs, γ, to be evaluated with *N* satellites in view is

$$\gamma_N = \sum_{k=4}^{N} \binom{N}{k}\binom{k}{2}. \quad (6)$$

4.2 IONOSPHERE-INDUCED RANGE ERROR

For each subset geometry, ionosphere-anomaly-induced errors are computed by simulating both stationary-ionosphere-front and fast-moving-ionosphere-front scenarios. The ionosphere-induced range error is computed by assuming that the two satellites generating (as a pair) the largest ionosphere-induced error are impacted simultaneously by the front. This is denoted as the "double-satellite-impact" scenario. Because the worst-case pair is not known a-priori, a search of all independent pairs is carried out by the simulation.

Case (1) Stationary Ionosphere Front Scenario

The MIEV module generates two "sub-cases" for each satellite pair (k_1, k_2): the "k_1-worst" and the "k_2-worst" cases. For the "k_1-worst" case, the worst stationary-case-scenario is applied to satellite k_1, and then the corresponding moving-front-scenario with consistent front velocity and direction is applied to satellite k_2 as shown in Figure 9. Let us denote the range errors of satellites k_1 and k_2 for the "k_1-worst" stationary case respectively as:

$$\varepsilon_{I,k1,1} \quad , \quad \varepsilon_{I,k2,1}. \quad (7)$$

This worst-stationary case takes place when the ionosphere front hits ionosphere-pierce-points (IPP) of two satellites simultaneously, the ionosphere front orientation is perpendicular to the runway orientation, and the velocity of the IPP in the runway direction is identical to the velocity of the ionosphere front. In other words, when the IPP velocity of satellite k_1 projected into the runway direction, $V_{k1,proj}$, is equal to the ionosphere-front velocity, V_{front}, this front appears to be stationary with respect to LGF and satellite k_1. The range error on satellite k_1 (which can be found from the 3-D MIER lookup table described in Section 3.2) is

$$\varepsilon_{I,k1,1} = f_{Table}(dV_{front/IPP,k1}, V_{front}, El_{k1}). \quad (8)$$

where $dV_{front/IPP,k1} = 0$ (i.e., creating a "stationary front" from the point-of-view of the LGF), $V_{front} = V_{k1,proj}$, and El_{k1} is the elevation angle of satellite k_1.

Because the IPP velocities of two satellites are almost always different, an ionosphere front cannot be stationary with respect to both satellites at the same time given that the front crosses the IPPs of both satellites concurrently. By orienting the front to be worst-case for satellite k_1, the velocity of the front with respect to the LGF and satellite k_2 almost always becomes non-zero (i.e., moving) and is always deterministic. By taking the IPP velocity of satellite k_2 into account, the ionosphere-front velocity with respect to the IPP motion of the satellite k_2 is computed as:

$$dV_{front/IPP,k2} = V_{k1,proj} - V_{k2,proj}. \quad (9)$$

Only when the ionosphere front moves faster than the IPP of satellite k_2 (i.e., when $dV_{front/IPP,k2}$ is positive) can the range error on satellite k_2 have a non-zero value [8]. The range error on satellite k_2 in this case is:

$$\begin{aligned} &\varepsilon_{I,k2,1} = f_{Table}(dV_{front/IPP,k2}, V_{front}, El_{k2}) \\ &\varepsilon_{I,k2,1} = 0, \quad if \quad dV_{front/IPP,k2} < 0 \end{aligned}. \quad (10)$$

where $V_{front} = V_{k1,proj}$ and El_{k2} is the elevation angle of satellite k_2.

For the "k_2-worst" case, the "k_1-worst" case is simply reversed. Now, the worst-stationary-case-scenario is applied to satellite k_2, and then the corresponding moving-front-scenario with consistent front velocity and direction is applied to satellite k_1. Let us denote the range errors of satellites k_1 and k_2 for the "k_2-worst" stationary case to be, respectively:

$$\varepsilon_{I,k1,2} \quad , \quad \varepsilon_{I,k2,2}. \quad (11)$$

The ionosphere front is stationary with respect to LGF and the satellite k_2 in this scenario. Thus, $V_{front} = V_{k2,proj}$, $dV_{front/IPP,k2} = 0$ and the resulting range error on satellite k_2 is

$$\varepsilon_{I,k2,2} = f_{Table}(dV_{front/IPP,k2}, V_{front}, El_{k2}). \quad (12)$$

The relative velocity of the ionosphere front with respect to the IPP of satellite k_1 is computed as:

$$dV_{front/IPP,k1} = V_{k2,proj} - V_{k1,proj} \tag{13}$$

From the lookup table, the range error on satellite k_1 is

$$\varepsilon_{I,k1,2} = f_{Table}(dV_{front/IPP,k1}, V_{front}, El_{k1})$$
$$\varepsilon_{I,k1,2} = 0, \quad if \quad dV_{front/IPP,k1} < 0 \tag{14}$$

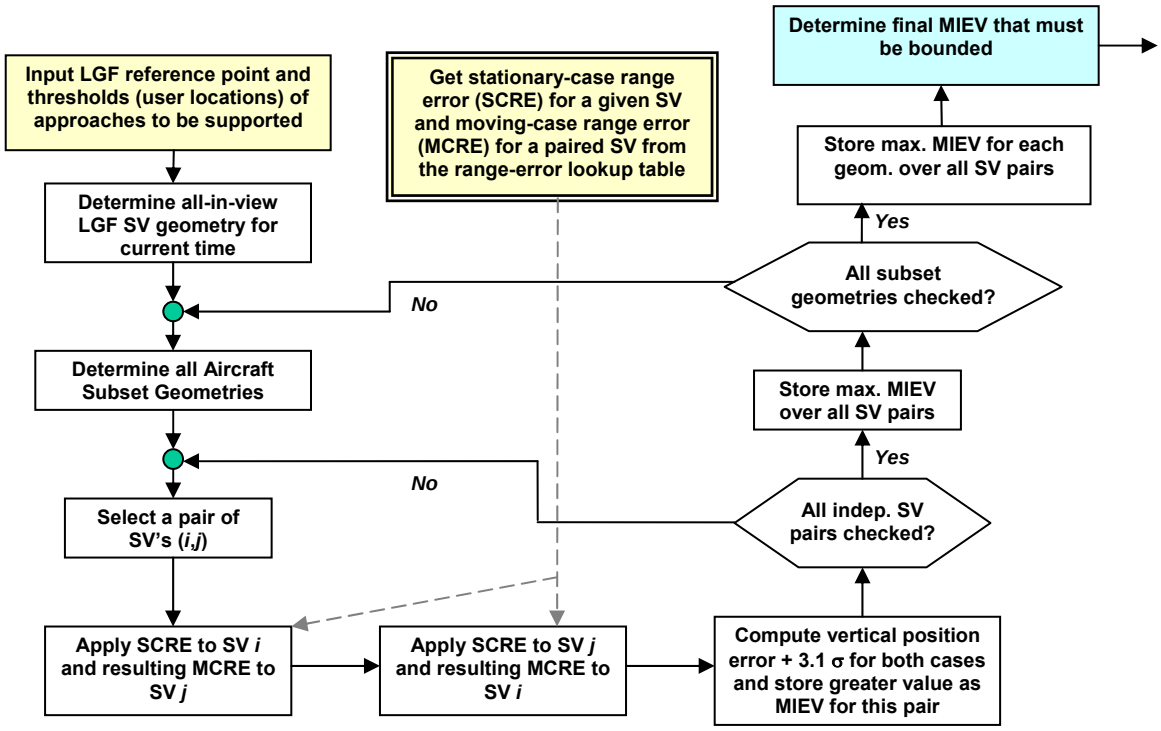

Figure 8: Flow Chart for Stationary-Ionosphere-Front Scenario

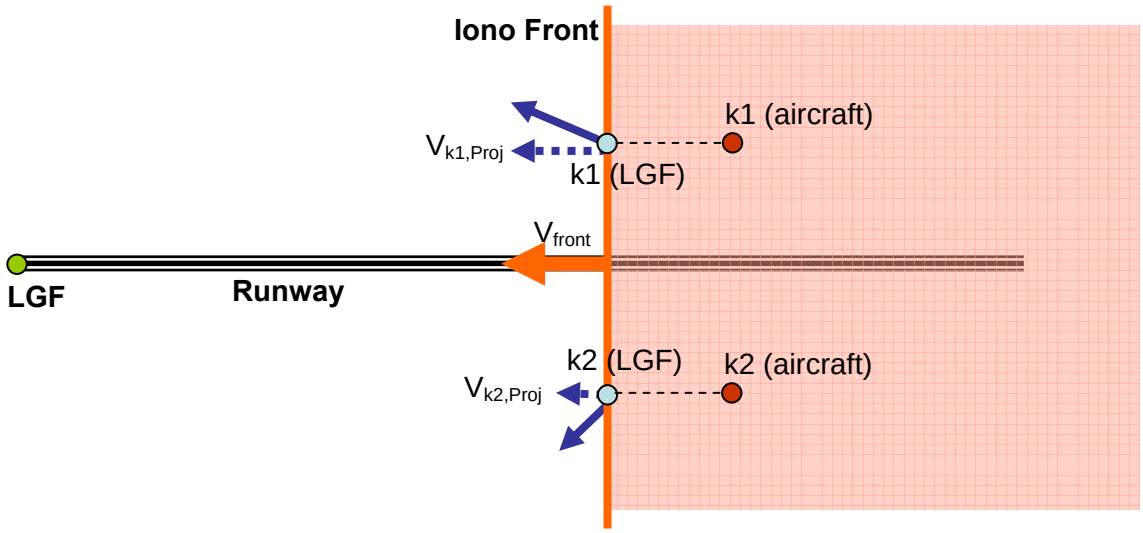

Figure 9: "k_1-worst" Case of Stationary-Ionosphere-Front Scenario

Case (2) Fast-Moving Ionosphere Front Scenario

In the previous subsection, a simulation method was described for the stationary ionosphere front scenario for which the resulting user impacts are expected to be severe since the underlying anomalies cannot be detected or mitigated by LGF CCD monitoring. Once the ionosphere front starts to move relative to the IPP motion, the possibility of detection increases because the CCD monitor observes the ionosphere delay rate-of-change over time. However, the maximum possible user error may also become larger based on the ionosphere threat model (see Section 2.0) since the maximum ionosphere gradient increases as the ionosphere front speed increases. Therefore, the likelihood of detection and the maximum range error increase compete as the ionosphere front speed increases, and there exists a specific speed relative to the satellite which results in the worst range error on that satellite. This speed is denoted as *dV* and can be obtained from the delta-V lookup table (see Section 3.2) for a given IPP speed and satellite elevation angle.

An approach almost identical to that for the stationary ionosphere front scenario is taken for the fast-moving-ionosphere-front scenario. As for the stationary-front scenario, the MIEV module generates two sub-cases for each satellite pair (k_1, k_2): the "k_1-worst" and the "k_2-worst" cases. For the "k_1-worst" case, the worst-case moving-front scenario is applied to satellite k_1, and then the corresponding moving-front-scenario with consistent front velocity and direction is applied to satellite k_2. The range errors of satellites k_1 and k_2 for the "k_1-worst" moving case are defined respectively as:

$$\varepsilon_{I,k1,3} \quad , \quad \varepsilon_{I,k2,3} \; . \tag{15}$$

With a known elevation angle, El_{k1}, and the IPP velocity projected into the runway direction, $V_{k1,proj}$, of satellite k_1, the front speed relative to the IPP speed which produces the worst range error to satellite k_1 is determined using the delta-V table for the LGF-to-user separation being analyzed:

$$dV_{front/IPP,k1} = dV_{Table}(V_{IPP,k1}, El_{k1}) \tag{16}$$

where $V_{IPP,k1}$ is equal to $V_{k1,proj}$. Then the ionosphere-front speed with respect to the ground is

$$V_{front} = dV_{front/IPP,k1} + V_{k1,proj} \; . \tag{17}$$

The range error on satellite k_1 (from the MIER lookup table) is

$$\varepsilon_{I,k1,3} = f_{Table}(dV_{front/IPP,k1}, V_{front}, El_{k1}) \; . \tag{18}$$

By setting the front speed to be the worst-case speed with respect to satellite k_1, the velocity of the front with respect to the LGF and satellite k_2 becomes fixed and deterministic. Next, by taking the IPP velocity of satellite k_2 into account, the ionosphere-front velocity for satellite k_2 is computed as:

$$dV_{front/IPP,k2} = V_{front} - V_{k2,proj} \; . \tag{19}$$

The range error on satellite k_2 (which can be obtained from the lookup table) is

$$\begin{aligned} &\varepsilon_{I,k2,3} = f_{Table}(dV_{front/IPP,k2}, V_{front}, El_{k2}) \\ &\varepsilon_{I,k2,3} = 0, \qquad if \quad dV_{front/IPP,k2} < 0 \end{aligned} \; . \tag{20}$$

For the "k_2-worst" scenario, the range errors of satellites k_1 and k_2 are denoted respectively as:

$$\varepsilon_{I,k1,4} \quad , \quad \varepsilon_{I,k2,4} \; . \tag{21}$$

The resulting ionosphere-induced errors are computed using the following equations, which are almost the same as those described for the "k_1-worst" case except for the swapping of the k_1 and k_2 indices:

$$\begin{aligned} &dV_{front/IPP,k2} = dV_{Table}(V_{k2,proj}, El_{k2}); \\ &V_{front} = dV_{front/IPP,k2} + V_{k2,proj}; \\ &\varepsilon_{I,k2,4} = f_{Table}(dV_{front/IPP,k2}, V_{front}, El_{k2}); \\ &dV_{front/IPP,k1} = V_{front} - V_{k1,proj}; \\ &\varepsilon_{I,k1,4} = f_{Table}(dV_{front/IPP,k1}, V_{front}, El_{k1}); \\ &\varepsilon_{I,k1,4} = 0,, \qquad if \quad dV_{front/IPP,k1} < 0. \end{aligned} \tag{22}$$

4.3 MAXIMUM-IONOSPHERE-INDUCED-ERROR-IN-VERTICAL (MIEV)

Maximum-Ionosphere-induced-Error-in-Vertical (MIEV) is computed by adding K_{MD} sigma of nominal vertical position error to ionosphere-induced error (K_{MD} is assumed to be 3.1, representing an implied missed-detection probability of 0.001 from a one-sided standard Gaussian distribution):

$$\begin{aligned} MIEV_{k1,k2,P} &= \left| S_{vert,k1}\varepsilon_{I,k1,P} + S_{vert,k2}\varepsilon_{I,k2,P} \right| \\ &+ K_{MD}\sqrt{\sum_{i=1}^{N_c} S_{vert,i}^2 \sigma_i^2}; \quad P = 1,2,3,4 \end{aligned} \tag{23}$$

where $S_{vert,}$ is the row of the weighted-least-squares projection matrix corresponding to the vertical position state, N_c is the number of satellites used in the position fix, and σ_i is the standard deviation of the remaining (nominal) error sources (which includes ground, air, and troposphere errors). Note that the four possible integer values of the index variable *P* represent the four cases evaluated in Section 4.2. The maximum MIEV over all satellite pairs and threat scenarios is stored for each possible subset geometry:

$$MIEV_S = \max(MIEV_{k1,k2,P}); \qquad S = 1, 2, ..., \alpha . \qquad (24)$$

The use of the α MIEV values in the vector $MIEV_S$ in determining required sigma inflation factors is described in Section 4.4.

4.4 INFLATION FACTOR FOR A SINGLE EPOCH

When describing inflation factor determination, it should be noted that both σ_{pr_gnd} inflation and σ_{vig} inflation are included. σ_{pr_gnd} inflation is used to provide a required initial level of sigma inflation needed regardless of the current constellation, aircraft location, or even the occurrence of ionosphere anomalies. The minimum inflation of 2.5 for σ_{pr_gnd} would likely be needed to provide protection from other anomalies such as the non-Gaussian behavior of pseudorange correction errors, signal deformations, and ephemeris errors. σ_{vig} inflation is the best way to protect aircraft at LGF separations beyond the CAT I approach Decision Height (DH) (refer to Section 4.5 for more details).

The broadcast sigma inflation factors for σ_{pr_gnd} and σ_{vig} are determined so that all intolerable "subset" geometries are excluded at the aircraft by inflating VPL to exceed the "normal" VAL (not $VAL_{H2,I}$, which is only known to the LGF's offline simulation procedure). The steps to determine inflation factors required at a time of incident are as follows:

a. Initialize a fixed inflation for σ_{pr_gnd}, i.e., I_{pr_gnd} = 2.5 as a default value. This inflation factor is defined relative to σ_{pr_gnd} as a function of satellite elevation angle as given by the Ground Accuracy Designator (GAD) C3 LGF error model given in [10].

b. Divide all subset geometries into two categories: Subset *A* if MIEV is less than $VAL_{H2,I}$; and Subset *B* if MIEV is greater than $VAL_{H2,I}$.

c. If the distance from the LGF to a user location, x, is less than that of the LGF to the DH, increase the σ_{vig} inflation factor, I_{vig}, in steps of ΔI_{vig} until all geometries in Subset *B* satisfy the following condition:

$$VPL_{H0,I}(\sigma_{pr\_gnd,I}, \sigma_{vig,I}) > VAL \qquad (25)$$

where $\sigma_{pr\_gnd,I} = I_{pr\_gnd}\sigma_{pr\_gnd}$, $\sigma_{vig,I} = I_{vig}\sigma_{vig}$, $VPL_{H0,I}$ is the inflated VPL, and VAL is the "normal" vertical alert limit at x km (as specified in Table B-69 of the RTCA LAAS MOPS [4]).

d. If x is beyond the separation between the LGF and the DH, increase the σ_{vig} inflation factor, I_{vig}, in steps of ΔI_{vig} until all geometries in Subset *B* satisfy the following condition:

$$VPL_{H0,I}(\sigma_{pr\_gnd,I}, \sigma_{vig,I}) > VAL$$
$$or \qquad (26)$$
$$2.0\,\sigma_{vert}(\sigma_{pr\_gnd,I}, \sigma_{vig,I}) > FASVAL$$

The second condition in Equation (26) is added to utilize the Bias Approach Monitor (BAM) requirement specified in Section 2.3.11.5.2.2 of the RTCA LAAS MOPS [4]. σ_{vert} is the vertical error standard deviation computed using the inflated σ_{pr_gnd} and σ_{vig}, and *FASVAL* is equal to 10 meters at all separations.

e. Store $I_{vig}(x,t)$ and I_{pr_gnd}, where *x* is the LGF-to-user separation and *t* is the time of epoch.

4.5 SIGMA INFLATION TO SUPPORT LAAS COVERAGE AREA

In order to ensure that $VAL_{H2,I}$ bounds MIEV for all usable "subset" geometries for LGF-to-aircraft separations beyond that of the CAT I approach DH, the simulation described above should be repeated to cover all distances from the LGF to a value corresponding to 10 nautical miles (18.7 km) beyond the furthest CAT I DH being supported by that LGF. This requirement induces additional sigma inflation beyond what is needed at any given DH. Inflation of σ_{pr_gnd} alone would cause a significant loss of availability since an excessive value of σ_{pr_gnd} is required as the LGF-to-user separation increases. This is the reason for inflating σ_{vig} in addition to inflating σ_{pr_gnd} in Section 4.4. Because the impact of σ_{vig} inflation on VPL_{H0} at the aircraft naturally increases with LGF-to-aircraft separation, inflation of this parameter beyond the nominal value of 4 mm/km is the best way to implement this additional inflation.

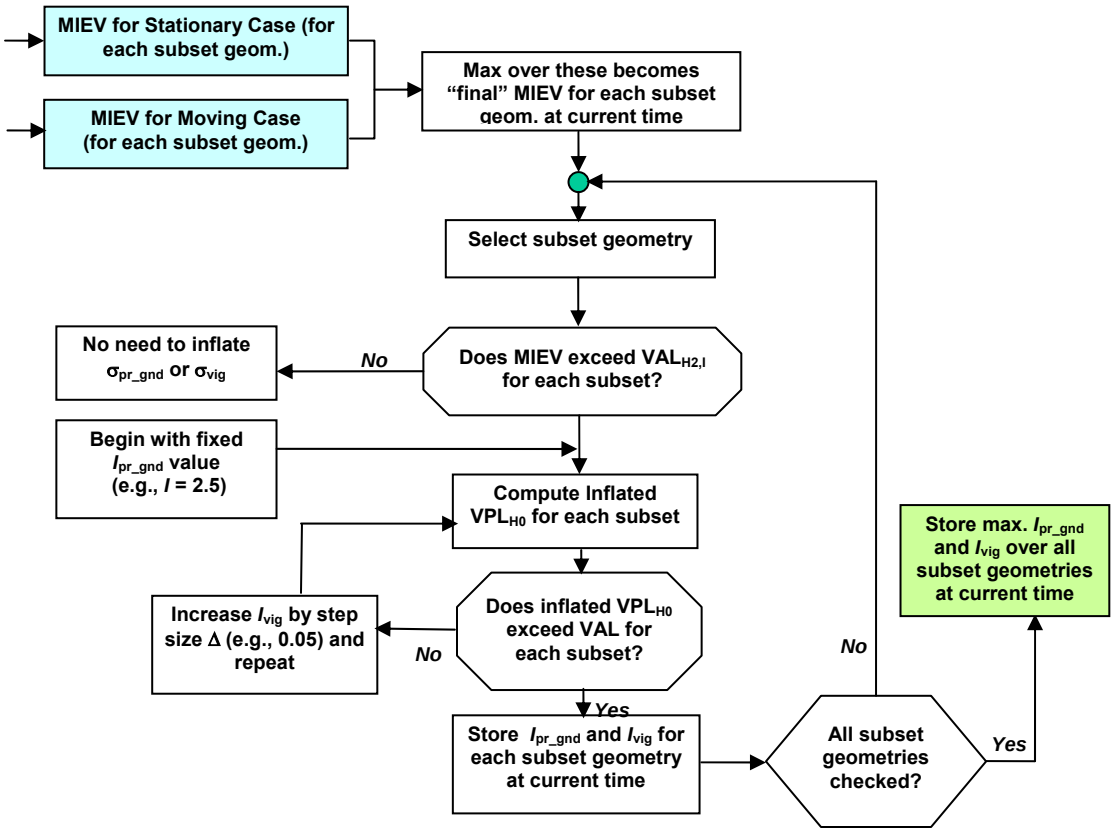

Figure 10: Flow Chart for Inflation Factor Determination (Part 1)

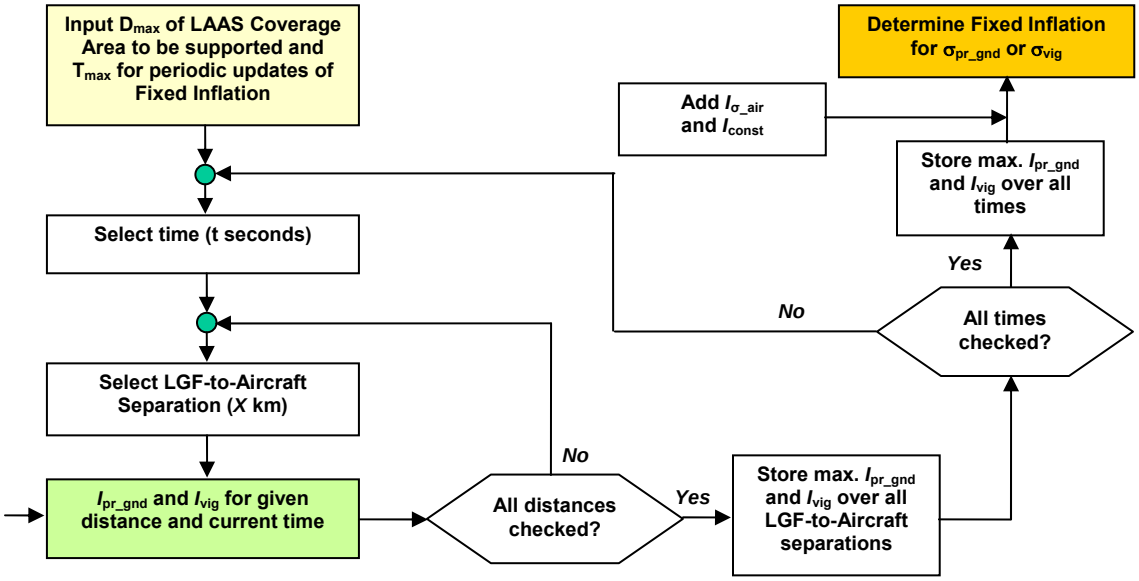

Figure 11: Flow Chart for Inflation Factor Determination (Part 2)

The steps to determine sigma inflation factors which support the LAAS coverage area at a single epoch in time are as follows:

a. Repeat simulation algorithms described in Section A-4.2 – A-5.2 for each distance, x, in steps of Δx, out to the maximum value ($x_{max} = x_{DH\_max}$ + 18.7 km).

b. Store the maximum I_{vig} and I_{pr_gnd} over all distances.

$$I_{vig}(t) = \max\left\{I_{vig}(x,t)\right\}, \qquad I_{pr\_gnd}; \quad x = 1, 1+\Delta x, ..., x_{\max} \tag{27}$$

4.6 FIXED SIGMA INFLATION DETERMINATION

The final sigma inflation factors over all epochs within a 24-hour day of repeatable GPS geometries are determined through the following steps.

a. Repeat simulation algorithms in Sections 4.1 – 4.5 for each epoch, t, in steps of Δt, between t = 0 and t = 24 hours.

b. Store the maximum I_{vig} and I_{pr_gnd} over all epochs.

$$I_{vig} = \max\left\{I_{vig}(t)\right\}, \qquad I_{pr\_gnd}; \quad t = 0, \Delta t, ..., t_{final} \tag{28}$$

4.7 ADDITIONAL INFLATION FACTORS

1) *Inflation to cover the uncertainty of the airborne error model (I_{σ_air})*

The airborne error model (σ_{air}) that the aircraft might use is not completely known to the LGF. If the LGF chooses a specific airborne error model to compute geometry weighting and nominal errors, the resulting MIEV and VPL might be different from the actual MIEV and VPL which the aircraft might have in real time. Therefore, additional inflation might be needed to cover the uncertainty of the airborne error model. This would be determined by running additional simulations with a range of possible values of σ_{air} that do not match the LGF assumptions for σ_{air}. If necessary, the uncertainty is then covered by inflating I_{pr_gnd} or I_{vig} with the additional inflation factor, I_{σ_air}, to cover the maximum additional degree of inflation required by the most conservative of these additional simulations.

2) *Inflation to cover GPS constellations creating geometries worse than those bounded by offline simulation (I_{const})*

Offline simulation must include a set of GPS constellations to derive inflation factors that are sufficiently robust to GPS constellation variations between infrequent updates of the inflation factors (more details are in Section 5.0). Since it is impossible to predict future GPS constellations with any reliability, a small additional inflation factor, e.g., I_{const}, is needed. Adding more satellites to the GPS constellation tends to increase I_{vig} because it creates more permutations of marginal subset satellite geometries that I_{vig} inflation must protect against. In practice, adding more satellites also makes these marginal subset geometries much less likely, but the LGF cannot take credit for this – it must still protect all usable subsets down to 4 satellites.

5.0 RESULTS AND DISCUSSION

This section presents an example result of the MIEV and sigma-inflation-determination simulations. The standard RTCA 24-satellite GPS constellation (as specified in Table B-1 of the RTCA WAAS MOPS, DO-229C [10]) was simulated at Memphis for 24 hours with a time interval (Δt) of five minutes, giving 288 independent sets of "all-in-view" (to an LGF at a given location) satellite geometries. The mitigation provided by the LGF CCD monitor was taken into account for this analysis as described in Section 3.0.

The green curve in Figure 12 shows the original (un-inflated) VPL of all-in-view geometries at the Decision Height (DH) of 5 km from the LGF for a given epoch. The blue diamonds indicate the maximum ionosphere-induced error out of all two-SV-impacted combinations for each time epoch. Both stationary-ionosphere-front and moving-ionosphere-front scenarios were simulated for each combination, as described in Section 4.2. The MIEV of the all-in-view geometry at each epoch was computed by adding nominal errors to the ionosphere-induced errors for that geometry. The all-in-view MIEV is shown as the grey curve (with stars for points) in Figure 12. For all-in-view geometries, MIEV is always bounded by $VAL_{H2,I}$ (which is 24 meters at the DH); thus no sigma inflation is needed to protect them.

In addition to the all-in-view geometry, the LGF must consider all possible subset geometries that might be used by the aircraft for its position fix. One of these subset geometries is the "driving" geometry that determines the sigma inflation factor at a given epoch and LGF-to-user separation, and in almost all cases, the driving geometry requires at least some inflation of σ_{vig} given the fixed amount of σ_{pr_gnd} inflation (i.e., I_{pr_gnd} = 2.5) already applied. Figure 13 shows an example result of sigma inflation determination for a single epoch. Among subset

geometries at Epoch 157 from Figure 12, those for which MIEV exceeds $VAL_{H2,I}$ and VPL_{H0} is below the standard 10-meter (FAS)VAL are shown here. These subsets with unacceptable errors are the ones which require additional sigma inflation. The inflation factor for σ_{vig} (or I_{vig}) was increased until the inflated VPL_{H0} of all troublesome geometries exceeded the VAL of 10 meters. For this epoch, the required I_{vig} was 2.43 (given I_{pr_gnd} of 2.5).

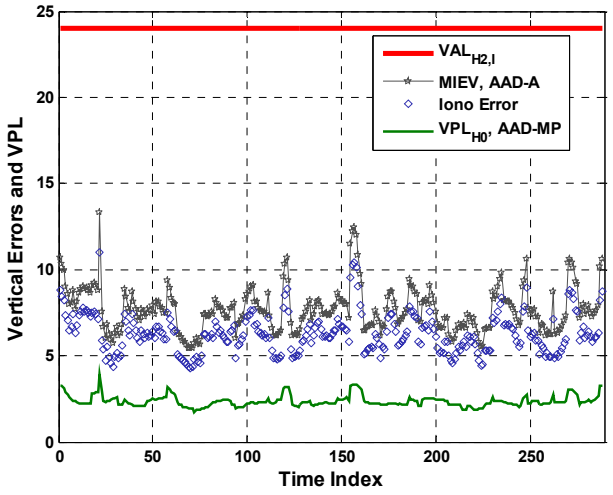

Figure 12: MIEV simulation results of all-in-view geometries at Memphis using RTCA 24-SV constellation

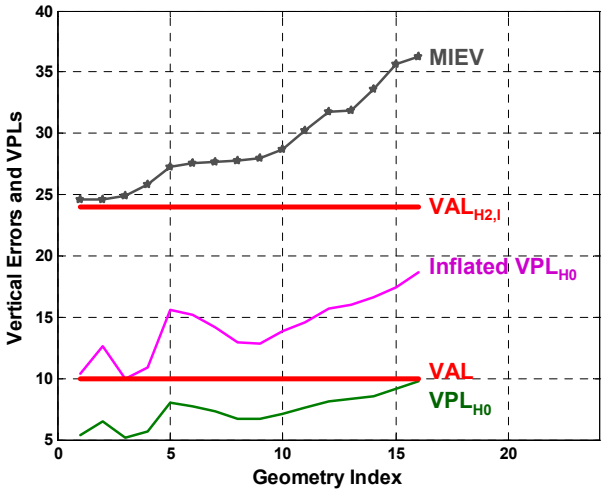

Figure 13: Example result of sigma inflation determination for a single epoch

Figure 14 shows the required inflation factors for σ_{vig}, I_{vig}, at each epoch and a given LGF-to-aircraft distance at Memphis. I_{vig} was determined to protect users against ionosphere anomalies given the pre-fixed I_{pr_gnd} of 2.5. The different markers of the curves represent different LGF-to-user separation distances. Considering the furthest DH to be 5 km from the LGF, 5 km plus 10 n.mi. (or 23.7 km) from the LGF represents the edge of the Precision Approach Region for this airport. Simulations for five discrete distances (3, 5, 8, 12 and 20 km) were performed to determine the inflation factors using the corresponding $VAL_{H2,I}$ value from Figure 1 and MIER lookup table (as described in Section 3.2) at each distance. Recall that an acceptable pair of I_{pr_gnd} and I_{vig} makes all subset geometries with unacceptable errors (i.e., MIEV > $VAL_{H2,I}$) unavailable to users by increasing VPL_{H0} to exceed VAL. Because of changes in satellite geometry, the minimum sufficient value of I_{vig} varies with time given that I_{pr_gnd} is fixed. I_{vig} also depends on LGF-to-user separation, mainly because ionosphere-induced errors increase with additional separation. However, no dominating separation (i.e., a separation which always requires the highest inflation factor) is seen because of the complex variation of the example $VAL_{H2,I}$ curve with separation in Figure 1.

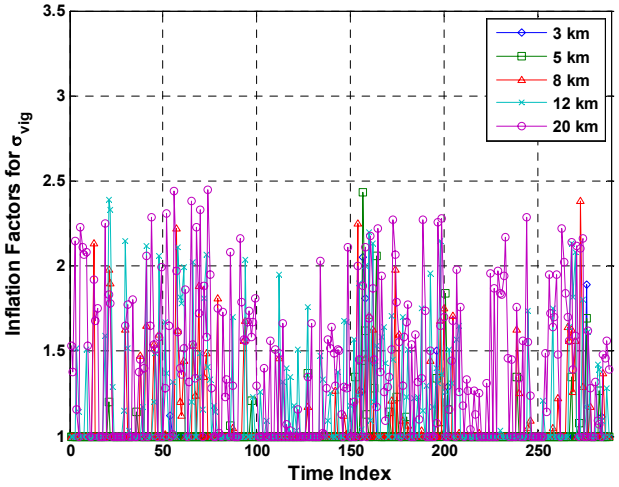

Figure 14: Real-Time Inflation Factors for σ_{vig} at Memphis (based on Example $VAL_{H2,I}$ Curve)

Because the likely choice of airborne error models is constrained by the RTCA LAAS MOPS to only two choices, Airborne Accuracy Designator (AAD)-A and (lower-error) AAD-B, both of which include the same airborne multipath error model AAD-MP [4], little to no additional inflation is needed to cover this variation if the LGF uses conservative choices for airborne error models when computing VPL_{H0} and MIEV. For this reason, MIEV was calculated based on AAD-MP and AAD-A to give the most-severe airborne error model consistent with the MOPS. This has the impact of maximizing MIEV and thus making more subset geometries potentially hazardous; thus it is the most conservative choice of airborne error models consistent with the MOPS. Conversely, when inflated (or un-inflated, when I_{vig} and

I_{pr_gnd} = 1.0) VPL_{H0} is computed as shown in Figures 12 and 13, the least-severe error model consistent with the MOPS is used, which is AAD-MP by itself without either the AAD-A or AAD-B noise contributions. This has the effect of minimizing VPL and thus requiring higher inflation factors to make the same unsafe geometries unusable at the aircraft.

Availability at Memphis was evaluated with fixed sigma inflation, as shown in Figure 15. Fixed sigma inflation means that, instead of the varying value of I_{vig} with time shown in Figure 14, the maximum value of I_{vig} over all epochs and LGF-to-user separations, which is 2.45, is used for all epochs along with the (always fixed) I_{pr_gnd} = 2.5. This pair of fixed inflation factors was applied to compute the inflated VPL_{H0} (shown as the pink curve) of all-in-view geometries at the DH. The result shows that an availability of 99.9 % is achievable at Memphis using fixed sigma inflation with significant margin (e.g., the maximum inflated VPL_{H0} is about 8 meters, which is significantly lower than the FASVAL of 10 meters) for GPS constellations with satellite outages. The estimated availabilities at Los Angeles and Minneapolis/St. Paul airports using the same approach were slightly better than one shown here for Memphis.

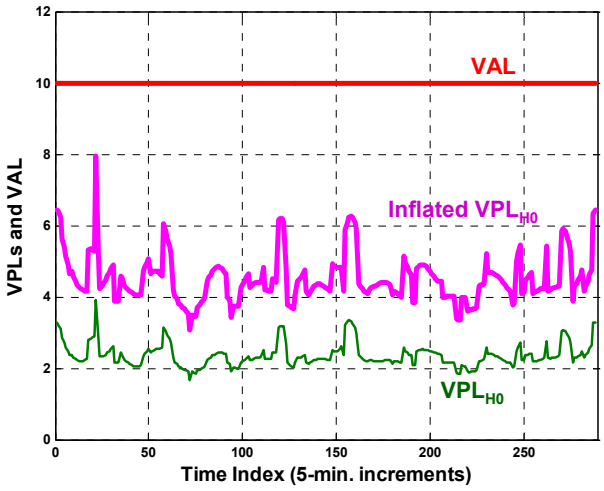

Figure 15: "Ideal" Availability at Memphis with Fixed Inflation (using Example $VAL_{H2,I}$ Curve)

Because the GPS constellation changes with time, sigma inflation factors cannot be set for all time but must instead be re-calculated at infrequent but regular intervals. In order to assess the variation of I_{vig} over time while keeping a constant I_{pr_gnd} of 2.5, simulations were conducted for a series of old, recent, and proposed future GPS constellations based on Yuma almanacs downloaded from the U.S. Coast Guard NAVCEN website [11], and the results are shown in Table 3.

In terms of choosing an interval between updating fixed-inflation-factor simulations and the value of I_{vig} prior to the next update, it helps to distinguish between two factors that can change I_{vig} over time. One is the normal *drifting* of satellites within and around their desired nominal orbit slots over time. Accompanying drifting as a feature of normal constellation operation is the use of variable spare orbit slots when new satellites are launched to planes with all primary orbit slots occupied. We can see the effect of drifting and spare slots by examining the variation among the eight inflation factor results shown between August 2003 and August 2006 in Table 3. In percentage terms (i.e., [max – min] / min × 100%), these results cover a range of 13.8%. Therefore, if a 3-year inflation update rate were chosen, we could cover the drifting-and-sparing effect with a 15% range over the results of the previous 3 years. To cover both possibilities, we propose choosing a fixed I_{vig} to cover drifting and sparing for the next 3-year period by selecting the greater of (a) the maximum I_{vig} over the most recent 3-year period (sampled at 6-to-8-month intervals plus the most recent available GPS almanac) or (b) the value of I_{vig} determined for the most recent almanac inflated by 10%, or two-thirds of the total range. For the numbers in Table 3, the maximum over the past three years is 3.13 (from August 2003), while the value from the most recent almanac (mid-August 2006) is 2.89, which when increased by 10% (i.e., multiplied by 1.10) becomes 3.18. Therefore, the larger of these two values, I_{vig} = 3.18, would be the candidate fixed I_{vig} inflation factor based on normal drifting and sparing phenomena.

Date and Constellation Description	Resulting I_{vig}
28-SV Const. from August 2003	3.13
29-SV Const. from April 2004	2.94
30-SV Const. from January 2005	2.93
29-SV Const. from September 2005	3.02
29-SV Const. from March 2006	2.75
29-SV Const. from June 2006	2.85
29-SV Const. from early August 2006	2.88
29-SV Const. from mid-August 2006	2.89
Proposed Future 30-SV (6-plane) Const. from [15]	3.16

Table 3: σ_{vig} Inflation Factors for Various GPS Constellations over Time

The second factor that changes I_{vig} over time is harder to foresee in advance. Major changes to the GPS constellation over time, such as shifts in the nominal orbit slots of GPS satellites due to transitioning to a greater or lesser number of primary satellites in the constellation and/or a shift from 6 to 3 orbit planes, could significantly change the required inflation factors. Without knowing the specifics of future constellation changes, it is difficult to foresee how much the needed I_{vig} might change, but a hint exists in Table 3. A reasonable upper bound as to what might be approached in the next several years is given by the 6-plane, 30 satellite constellation originally proposed by Massatt and Zeitzew in 1998 [12]. While it is unlikely that even this constellation could be achieved before Block IIF satellites became available in numbers in the 2011 – 2012 time frame, the value of I_{vig} that applies to it is 3.16, which we can use as an acceptable upper bound on the impact of GPS constellation expansion. This number is slightly smaller than the value of 3.18 that was selected above to cover drifting and spare orbit slots over the next three years; thus I_{vig} = 3.18 (the greater of the two I_{vig} numbers for drifting/sparing and expansion) is the number recommended for the next three years beginning in September 2006. Note that, if a one-year update interval were practical, I_{vig} could be reduced due to the smaller variation of I_{vig} between September 2005 and August 2006, but it would still exceed the value of 3.02 found from the September 2005 GPS constellation. Thus, the availability benefit would be small, but it would be measurable and potentially significant to users.

6.0 SUMMARY

This paper describes the process by which the ionosphere spatial anomaly threat is analyzed from past data, bounded in a threat model, simulated in multiple ways to determine the worst-case impact on CAT I LAAS users after considering the impacts of LGF CCD monitoring, and further mitigated by σ_{pr_gnd} and σ_{vig} inflation such that geometries that would be potentially hazardous to LAAS users are made unavailable. Based on the results of performing geometry screening simulations on several recent and not-so-recent GPS almanacs, a method for devising fixed σ_{pr_gnd} and σ_{vig} inflation factors and updating them every three years using offline simulation has been developed. Specific inflation factors have been proposed for the three-year period beginning in September 2006.

While the developed methodology should be usable for any LAAS system confronted by the threat of ionosphere anomalies, it should be made clear that the specific results in this paper only apply to CAT I LAAS operations inside CONUS. The threat model developed in Section 2.0 uses CONUS data only and thus does not necessarily cover ionosphere anomalies elsewhere in the world, particularly in equatorial regions where ionosphere activity is generally higher than it is in CONUS. In addition, the limited number of validated observations upon which the current CAT I CONUS threat model is based means that additional possible anomalies may exist that are not included in it. To address this concern, continued research into both the theory of ionosphere anomalies and data collected from these anomalies (both past and future) is recommended.

ACKNOWLEDGEMENTS

The constructive comments and advice regarding this work provided by many other people in the Stanford GPS research group are greatly appreciated. The authors would also like to thank Boris Pervan (IIT), John Warburton and Tom Dehel (FAA Technical Center), and Bruce DeCleene and Barbara Clark (FAA Aircraft Certification) for their help and advice. The authors gratefully acknowledge the Federal Aviation Administration Satellite Navigation LAAS Program Office for supporting this research. The opinions discussed here are those of the authors and do not necessarily represent those of the FAA or other affiliated agencies.

REFERENCES

[1] M. Luo, S. Pullen, S. Datta-Barua, G. Zhang, T. Walter, and P. Enge, "LAAS Study of Slow-Moving Ionosphere Anomalies and Their Potential Impacts," *Proceedings of the ION GNSS 2005*, Long Beach, CA., Sept. 13-16, 2005, pp. 2337-2339.

[2] M. Luo, S. Pullen, A. Ene, D. Qiu, T. Walter, and P. Enge, "Ionosphere Threat to LAAS: Updated Model, User Impact, and Mitigations," *Proceedings of the ION GNSS 2004,* Long Beach, CA., Sept. 21-24, 2004, pp. 2771-2785.

[3] B. DeCleene, "Performance Requirements for LPV Approaches to Minima as Low as 200 ft above Runway Threshold," International Civil Aviation Organization (ICAO) Navigation Systems Panel (NSP) Working Group 1 Meeting, Working Paper 55, Brussels Belgium, May 2006.

[4] *Minimum Operational Performance Standards for GPS Local Area Augmentation System Airborne Equipment*. RTCA, Washington, D.C., RTCA SC-159, WG-4A, DO-253A, Nov. 28, 2001.

[5] J. Lee, S. Pullen, S. Datta-Barua, and P. Enge, "Assessment of Nominal Ionosphere Spatial Decorrelation for LAAS," *Proceedings of the*

IEEE/ION PLANS, San Diego, CA, April 24-27, 2006.

[6] National Geodetic Survey (NGS) - CORS Data and Related Information. URL: http://www.ngs.noaa.gov/CORS/download2/

[7] A. Ene, D. Qiu, M. Luo, S. Pullen, and P. Enge, "A Comprehensive Ionosphere Storm Data Analysis Method to Support LAAS Threat Model Development," *Proceedings of the ION 2005 National Technical Meeting*, San Diego, CA, January 15-20, 2005, pp 110-130.

[8] *Algorithm Description Document for Ionosphere Anomaly Mitigation within the Local Area Augmentation System Ground Facility*. Stanford University LAAS Laboratory, Stanford, CA., Honeywell International, Coon Rapids, MN., Version 1.0, August 30, 2006.

[9] *Algorithm Description Document for the Code - Carrier Divergence Monitor of the Local Area Augmentation System*. Illinois Institute of Technology, Chicago, Illinois, November 2005.

[10] *Minimum Operational Performance Standards for GPS Wide Area Augmentation System Airborne Equipment*. RTCA, Washington, D.C., RTCA SC-159, WG-4, DO-245A, Nov. 28, 2004.

[11] GPS Almanac Archive, U.S. Coast Guard Navigation Center (NAVCEN) Web site, URL: http://www.navcen.uscg.gov/gps/almanacs.htm

[12] P. Massatt and M. Zeitzew, "The GPS constellation Design - Current and Projected," *Proceedings of the ION 1998 National Technical Meeting,* Long Beach, CA., Jan. 21-23, 1998.